A Bi-based artificial interphase to achieve ultra-long cycling life of Al-metal anode in non-aqueous electrolyte

Abstract: Rechargeable aluminum-ion batteries (RAB) with Al-metal anode are regarded as cost-effective and environmentally sustainable energy storage systems. However, tapping the high volumetric capacity of the Al-anode has been a challenge because of the spontaneous and irreversible formation of the oxide layer on its surface that renders it electrochemically inactive. Though recently reported $AlCl_3$-based electrolytes overcome this problem by breaking down this oxide layer, their highly corrosive nature hampers commercialization. Here, we investigate a novel approach to protect the Al-anode from severe oxidation by engineering an artificial protective interphase. A unique and less corrosive combination of $Al(CF_3SO_3)_3$ salt and $BiCl_3$ additive reacts with the Al-anode intrinsically to form an inorganic-rich protective bilayer. This layer is electronically insulating and significantly reduces the charge transfer resistance and surface activation energy at the anode, enabling plating/stripping at extremely low overpotential of <0.1 V that can be sustained for record-long cycling times of >4000 hours.

1. Introduction

Rechargeable batteries using metals as anodes are gaining popularity as an alternative to Li-ion batteries [1-6]. Metals like Li, Na, Zn, Mg, Ca, and Al offer higher volumetric capacity which make them suitable as an alternative to graphitic anodes [7], especially for smaller-sized batteries in portable applications. Factors such as initial investment cost, environmental sustainability, and limitations in the supply of Li prioritize non-Li chemistries for next-generation batteries. Among these, the rechargeable Al-ion battery (RAB) that uses high purity Al metal as an anode is the most promising because of its high volumetric capacity (~8000 mAh cm^{-3}), high abundance in the earth's crust, and the matured Al mining and recycling industry [8]. However, using Al metal as an anode in an electrochemical system has been traditionally challenging [9] because of the spontaneously-formed Al oxide layer. This passivating oxide layer is ionically insulating and has a high bandgap that makes the Al metal beneath electrochemically inert, effectively inhibiting low overpotential plating/stripping on its surface [10]. This overpotential can increase to as much as 5 V because of the oxide's presence, often causing undesirable electrolyte decomposition during cycling [11]. There are three strategies employed to bring down this excessive Al plating/stripping overpotential: (i) using $AlCl_3$-based electrolytes that can penetrate the passivating Al-oxide layer formed before or during the cycling [10], (ii) using a non-Al substrate that can facilitate low energy plating/stripping and guided deposition [12] and (iii) fabricating an artificial interphase on the Al anode to isolate and protect it from the side reactions, including severe oxidation [13-15]. All the three strategies have their pros and cons for an emerging battery research field like RAB.

Using $AlCl_3$-based electrolytes like anhydrous $AlCl_3$ + an ionic liquid (1-ethyl-3-methylimidazolium chloride (EMICl) or 1-butyl-3-methylimidazolium chloride) is highly effective but undesirably expensive; its corrosive nature further limits its usage on a large scale [10]. Despite cheaper alternatives such as $AlCl_3$ + urea and $AlCl_3$ + triethylamine hydrochloride being reported [16], the use of $AlCl_3$ continues to make the electrolytes corrosive. To avoid corrosion, haloaluminate-free electrolytes like $Al(OTf)_3$ in diglyme[17], N-methyl acetamide[18], urea[18] and tetrahydrofuran[19] have also been studied, but all of them show unsuccessful plating/stripping. Other studies with halide-free electrolytes including aluminum 1-butylimidazole bis(trifluoromethanesulfonyl)imide [20], $Al(TFSI)_3$ in acetonitrile [21] and $Al(PF_6)_3$ in dimethyl sulphoxide [22] show quasi-reversible plating/stripping often characterized by poor cycling stability and/or excessive side reactions. Additional electrolyte options, such as molten salts, gel-polymer electrolytes, and hybrid electrolytes, have also been investigated [10]. However, these alternatives present further demands, such as elevated

operating temperatures, incompatibility with current manufacturing facilities, and the need for lithium-containing cathodes, respectively. The results of the electrolyte-focused studies in the field of RABs[10] indicate the presence of Cl^- ions in the electrolyte to be indispensable in lowering overpotential and allowing for reversible plating/stripping.[23] This point is our overarching concern when designing our anode-electrolyte system. The halide ions are also crucial in the generation of charge carrying species like $AlCl_4^-$ which intercalate reversibly in the host materials[23-24].

The utilization of non-Al substrates is a highly effective solution for mitigating the challenges associated with large overpotential[12, 25]. In this approach, an optimal substrate is externally coated with Al and subsequently incorporated into the electrochemical system. However, this method necessitates additional steps and materials that may not be ideal from a commercialization standpoint. Furthermore, the anode capacity is constrained by the reservoir capacity of the substrate, imposing further limitations.

The strategy of protecting Al from severe oxidation and other side reactions by making a protective interphase involves two implementation approaches. An extrinsic approach focuses on modifying the Al anode outside the cell and utilizing the modified anode during cycling.[14] Techniques such as anode amorphization[26], anode alloying [27], and composite anodes [28] use this approach. The intrinsic approach involves modifying the Al anode within the cell. Methods such as fabricating concentrated electrolytes [29], introducing scavengers [30], and incorporating additives [31] are employed in this approach. The intrinsic approach offers an advantage as it can address corrosion and plating/stripping issues simultaneously by electrolyte modification, making it more relevant for RABs. However, for this strategy to be commercially viable, it is crucial to develop a cost-effective and facile methodology.

This study introduces a novel, facile method to mitigate severe oxidation and side reactions of the Al anode in a non-aqueous RAB electrochemical system. For the first time, we utilize the ion exchange reaction between Al and $BiCl_3$ ($Al + BiCl_3 \rightarrow Bi + AlCl_3$) to fabricate an artificial protective interphase on the Al anode (Fig. 1A). This interphase effectively maintains anode activity throughout cycling, preventing undesired reactions. We show that an intrinsic method of forming this protective interphase on the Al anode is the most effective, which was achieved by modulating aluminum trifluoromethanesulfonate ($Al(OTf)_3$) / 1,2-dimethoxyethane (DME) electrolyte with a small quantity (0.1 M) of inorganic additive, $BiCl_3$. To the best of our knowledge, $BiCl_3$ electrolyte additive has not been reported before in RAB, and provides the following unique benefits: (i) it spontaneously reacts with the Al anode to form a Bi-based artificial interphase with desirable anode-electrolyte surface properties, and (ii) it facilitates the generation of electroactive species in the electrolyte that are responsible for the reversible plating/stripping processes at the Al anode. This optimized electrolyte is less corrosive than commercial $AlCl_3$ + EMICl (3:2). Al plating/stripping study demonstrates a remarkable reduction in the overpotential to less than 0.1 V, which is sustained for unusually long periods of time (over 4000 hours), surpassing other results reported in the existing literature [10-11]. Through a comprehensive analysis of the anode-electrolyte interface, aided by the COMSOL simulations, we observed significantly improved interfacial properties that remained stable throughout multiple cycles of plating/stripping. Molecular dynamics (MD) simulations, conducted to investigate the evolution of the Al-ion solvation sheath, reveal desirable Al-Cl complexation upon the introduction of $BiCl_3$ in the electrolyte. Complementary materials characterization, including the use of a synchrotron, were employed to examine the evidence of Al plating/stripping and to decipher the composition and the material distribution on the surface of the cycled anode. A full cell with Bi-protected Al anode and $FeVO_4$ cathode is also demonstrated. Finally, we show that our general design strategy is applicable to magnesium-ion batteries as well.

2. Results

2.1 Propensity of Al plating/stripping in additive modulated electrolytes

Here, we study the propensity of Al to plate/strip in different additive-modulated electrolytes with cyclic voltammetry (CV) to determine the best formulation for the electrolyte. In agreement with published results [17-19], Al showed irreversible plating/stripping (Fig 1 B: grey curve) in a pure $Al(OTf)_3$ electrolyte in DME. The aluminated species were notably active as they plated during the negative scan, but no stripping was observed during the positive scan. Therefore we modified the 0.5 M $Al(OTf)_3$ electrolyte by adding small amounts (0.1 M) of additive. For this purpose, only metallic chloride salts ($SbCl_3$, $ZnCl_2$, $InCl_3$, $MgCl_2$, $CuCl_2$, $MoCl_2$ and $BiCl_3$) were chosen as the presence of Cl^- ion is found to be indispensable for successful plating/stripping (see Introduction). CV studies conducted in electrolytes with additives reveal that the plating/stripping behavior is dependent on the cation of the additive. For instance, the addition of $SbCl_3$ resulted in unstable plating/stripping during the positive scan, indicating excessive side-reactions (Fig. S1A). Conversely, stable cycling was observed in the presence of $ZnCl_2$, although it presented the possibility of multiple side reactions (Fig. S1B). The use of $InCl_3$ resulted in a lower stripping voltage, but stability could not be achieved (Fig. S1C). On the other hand, unsuccessful plating/stripping occurred when Mg, Cu, and Mo chlorides were present (Fig. S1D). Among the tested additives, the plating/stripping in the $BiCl_3$-modulated electrolyte stood out due to its relatively stable cycling (Fig. 1B). Furthermore, concentration optimization of $BiCl_3$ showed concentration-dependent stripping behavior (Fig. S2). Lower concentrations (e.g., 0.01 M and 0.05 M) exhibited excessive side reactions, as indicated by the broad curve during the positive scan. Similar broad curves with multiple peaks were observed for the 0.2 M and 0.5 M cases, suggesting the possibility of undesirable parasitic reactions with Al. The repetition of such reactions, as observed over 10 cycles, is undesirable as it can result in complete electrolyte decomposition. The plating/stripping behavior in the 0.1 M $BiCl_3$ + 0.5 M $Al(OTf)_3$ electrolyte (Fig. 1B) performed the best among the investigated additives and across different concentrations of $BiCl_3$ in terms of reversibility, stable cycling, and minimal occurrence of side-reactions. Comparing our CV curve with that of Reed et al. [32] in which they did not observe any plating/stripping in pure $Al(OTf)_3$-diglyme electrolyte due to passivation of Al anode, makes the crucial role of the $BiCl_3$ additive in regulating the Al surface chemistry clear. We speculate that the presence of $BiCl_3$ directly or indirectly helps in breaking the passivation layer on Al and maintains an active surface chemistry throughout the cycling. We additionally highlight that the CV curves obtained here for the optimized electrolyte exhibited a higher level of reversibility and stability, when compared to the modulation of $Al(OTf)_3$ with tetrabutylammonium chloride (TBAC) [11]. This indicates metallic chloride additives, specifically 0.1 M $BiCl_3$, to be a better choice as compared to organic chloride additives.

We also conducted controlled CV studies to investigate the potential involvement of non- Al ionic complexes in the plating/stripping processes. The irreversible plating/stripping curve observed in the $Al(OTf)_3$/DME electrolyte (Fig 1 B: grey curve) indicates that $Al(OTf)_3$ species do not participate in the plating/stripping phenomena. Similarly, a control CV study using the 0.1 M $BiCl_3$/DME electrolyte (Fig S3 A), which displays a linear current-voltage curve, ruled out the possibility of Bi-ion or its complexes being responsible for plating/stripping. Alternatively, the CV curve obtained from the 0.1 M $BiCl_3$ + 0.5 M $Al(OTf)_3$ electrolyte in Fig. 1B may indicate a reaction merely between the working electrode (here Pt) and the electrolyte. However, controlled CV studies using Ti and Mo substrates as the working electrodes demonstrated successful plating/stripping (Fig. S3B and C), thus confirming that the working electrode does not actively participate in the plating/stripping process. These controlled CV studies conclusively reject the possibility of non-Al species being involved in the plating and stripping reactions, as well as the activity of the working

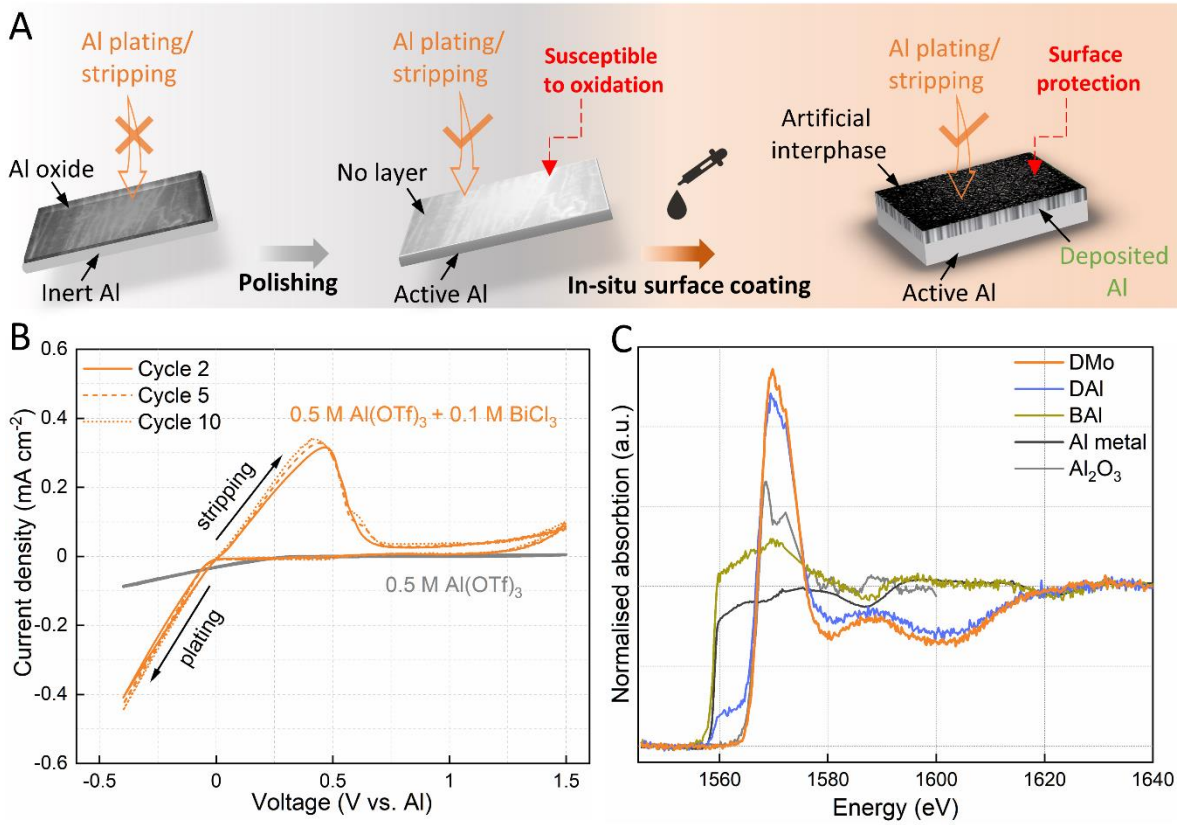

Fig. 1. The propensity of Al plating/stripping on protected Al metal. (**A**) Schematic illustration of the role of the artificial interphase in facilitating plating/stripping. (**B**) CV scan at 10 mV s^{-1} in 0.5 M $Al(OTf)_3$ vs 0.5 M $Al(OTf)_3$ + 0.1 M $BiCl_3$ electrolyte with Pt as working electrode, and Al as counter and pseudo reference electrode. (**C**) Al K-edge XANES spectra for DMo, BAl, DAl and standards Al_2O_3 and Al metal.

electrode. Therefore, the only remaining possibility is that of Al ions or Al-ion complexes being responsible for the observed plating/stripping behavior.

To gain insight into the nature of the plated species, we compared the X-ray Absorption Near Edge Structure (XANES) spectra (Fig. 1C) of different samples, including polished Al metal, Al_2O_3, BAl (polished Al metal dipped in 0.1 M of $BiCl_3$/DME solution for 10 mins), DAl (polished Al metal exposed to 0.1 M $BiCl_3$ + 0.5 M $Al(OTf)_3$/DME electrolyte) and DMo (Mo substrate plated in 0.1 M $BiCl_3$ + 0.5 M $Al(OTf)_3$/DME electrolyte). A prominent Al K-edge was observed in the XANES spectrum for the DMo sample, resembling the characteristic spectrum of Al_2O_3 and differing from that of pure Al metal. The rising edge of DMo overlaps with that of Al_2O_3 at 1567 eV, indicating the presence of an oxidized form of Al on the Mo substrate, likely in the +3-oxidation state [33]. Interestingly, the XANES spectrum of BAl closely resembles that of pure Al metal, suggesting that treating Al with $BiCl_3$ preserves the metallic nature of Al in the bulk, and the formation of Al^{3+} complexes does not occur (at least in the bulk) by reaction merely between Al and $BiCl_3$. However, in the presence of 0.1 M $BiCl_3$ + 0.5 M $Al(OTf)_3$ electrolyte, as observed for the DAl sample, the XANES spectrum exhibited rising edges corresponding to both metallic Al and Al^{3+}, confirming that the Al^{3+} species indeed originates from the electrolyte. These XAS findings provide valuable insights into the nature of the plated species and support the hypothesis of the electrodeposition of Al complexes (e.g., $Al_2Cl_7^-$), rather than simple Al^{3+} electroplating, in our experimental system. With the confirmation that Al can undergo reversible and stable plating/stripping in the 0.1 M $BiCl_3$ + 0.5 M $Al(OTf)_3$, we now turn our attention to exploring

the possibilities of reaction between Al and $BiCl_3$ in the context of using it to design a protective interphase on Al.

2.2 Designing protective interphase on Al

In this section, we study the modifications happening on the Al surface as a result of reaction between Al and $BiCl_3$. An Al metal surface was polished, cleaned and reacted with 0.1 M $BiCl_3$/DME solution and the structure and the composition of the modified surface was interrogated using scanning electron microscopy (SEM), energy dispersive X-ray spectroscopy (EDX), X-ray diffraction (XRD), and X-ray photoelectron spectroscopy (XPS).

A textured coating was formed when the Al surface reacted with $BiCl_3$ (Fig. 2A–B). From the cross-section view imaged by SEM, an interfacial layer rich in Al, Bi and Cl elements was observed on the Al substrate (Fig. 2C). The thickness of such a layer was observed to be dependent on the exposure time of Al metal to the $BiCl_3$/DME solution (Fig. 2D) and a uniform deposition is achieved at around 10 mins of reaction (Fig. S4). XRD analysis of Al coated for 10 mins (BAl) shows the presence of Bi metal (Fig. 2E) on the Al surface. However, XPS of BAl indicates the presence of $BiCl_3$, Bi_2O_3 and Bi (Fig. 2F) [34]. Upon etching, the relative amount of $BiCl_3$ is reduced significantly and only Bi_2O_3 & Bi are observed, indicating that the presence of $BiCl_3$ is merely due to unreacted reactants. The

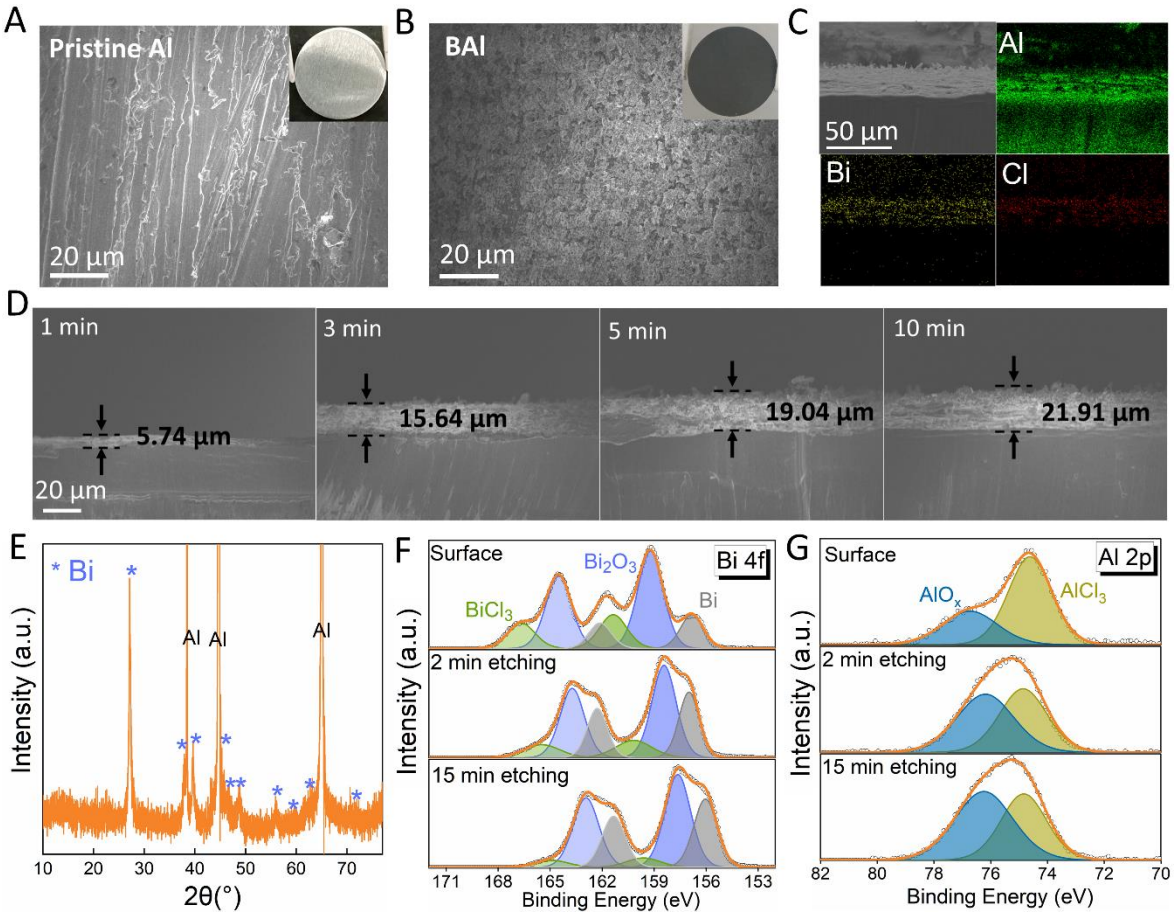

Fig. 2. Surface characterization of the artificial interphase fabricated on Al metal. SEM images of (**A**) Al foil and (**B**) Al foil treated with 0.1 M $BiCl_3$ for 10 mins (BAl). The insets of (A) and (B) are digital photos of Al foil and BAl. (**C**) Cross-sectional SEM image of a BAl and corresponding EDX mapping of Al, Bi, and Cl. (**D**) Cross-sectional SEM image Al foil treated with 0.1 M $BiCl_3$ for 1, 3, 5 and 10 mins. (**E**) X-ray diffractogram of BAl. (**F**) Bi 4f and (**G**) Al 2p region of XPS spectra for the surface and etched layers (2 & 15 min) of BAl.

existence of a small amount of Bi_2O_3 might originate from the oxidation of Bi metal during sample transfer or because of the reaction of Bi metal with some remnant oxygen in the $BiCl_3$ solution [34]. The XPS of BAl in the Al 2p region revealed the presence of $AlCl_3$ [35] and Al-oxide [36-39] on the surface and after etching. Notably, metallic Al, distinguishable by low energy peak at 72.6 eV [40-41], (Fig. S5) was not observed here. We also note here that, contrasting to the XPS of BAl, $AlCl_3$ was not detected in the XRD analysis. This can be because the surface of the BAl was rinsed with DME after the reaction to remove unreacted reactants and formed unattached products ($AlCl_3$ and excessive Bi in this case). XRD, being a bulk characterization technique, might not detect the traces of $AlCl_3$. Overall, the composition analysis of BAl indicates an ion exchange reaction between Al and $BiCl_3$ ($Al + BiCl_3 \rightarrow Bi + AlCl_3$) as evidenced by the presence of Bi and $AlCl_3$. Having established that the Al surface will react spontaneously via an ion exchange reaction with $BiCl_3$ and can form an artificial interphase on the bulk Al, we now proceed to investigate the best approach to exploit this reaction in terms of achieving superior plating/stripping reversibility and protection for the Al anode.

2.3 Implementation approaches to protect Al anode

In this section, we implement multiple approaches to fabricate a Bi-based protective coating on the Al anode and investigate the respective plating/stripping performance to ascertain the best solution. Approach I involves modifying the Al anode extrinsically, outside the cell by reacting it with 0.1 M $BiCl_3$ solution and utilizing the modified anode for cycling in a 0.5 M $Al(OTf)_3$ electrolyte. Approach II involves modifying the Al anode intrinsically by using a polished Al anode directly for cycling in a $BiCl_3$ modulated electrolyte, i.e. 0.1 M $BiCl_3$ + 0.5 M $Al(OTf)_3$. Approach III is a combination of Approaches I and II, which involves using an extrinsically-modified Al anode for cycling in $BiCl_3$-modulated electrolyte. Based on previous studies, all three methods have their own advantages, but as the best approach may be highly system dependent, we consider them individually here. Fig. 3A shows the comparative plating/stripping study of the three approaches. All the 3 approaches shows lower plating/stripping overpotential as compared to the Al symmetric cell cycled in 0.5 M $Al(OTf)_3$ (Fig. S6A). Approach II provides the best performance with a low overpotential of <0.1 V (10-fold better than Approaches I and III). Using extrinsically-modified Al resulted in a higher overpotential along with electrolyte decomposition, marked by the sloping curve rather than a flat plateau at the end of the charge and discharge cycles. Although cycling the extrinsically-modified Al in the Bi-modulated electrolyte stopped electrolyte decomposition, the low overpotential of cycling was not sustained and the cell failed in the 18^{th} cycle (35 hrs). Hence approach II is the preferred method here.

EIS study further demonstrates the effectiveness of the Bi-based protective coating and confirms Approach II as the best solution. All the three approaches show significantly reduced impedance as compared to Al-0.5 M $Al(OTf)_3$ system (Fig. 3B). Their EIS profiles also show a more kinetically controlled regime, indicating the enhanced role of the Al surface in controlling the charge transfer at the interface. The lowest impedance of ~1 kΩ is observed for the Al | 0.1 M $BiCl_3$ + 0.5 M $Al(OTf)_3$ | Al system, indicating the Al-anode surface to be ideally enhanced when modified intrinsically. The Tafel study (Fig. 3C) provides further insights as to the superiority of an intrinsic over an extrinsic approach. A higher exchange current density (46.46 μA cm^{-2} vs 0.24 μA cm^{-2}) is obtained with an intrinsic approach, with an exchange current density in the extrinsic coating as low as that of the Al | 0.5 M $Al(OTf)_3$ | Al system. We suspect the low exchange current density of the extrinsic approach to be due to the unavailability of haloaluminated ions like $Al_2Cl_7^-$ and $AlCl_4^-$ which are conventionally known to be the electroactive species for RAB [11]. Since there was no Cl^- ion present in the electrolyte with the extrinsic approach, electroactive species may not have formed. Thus, the

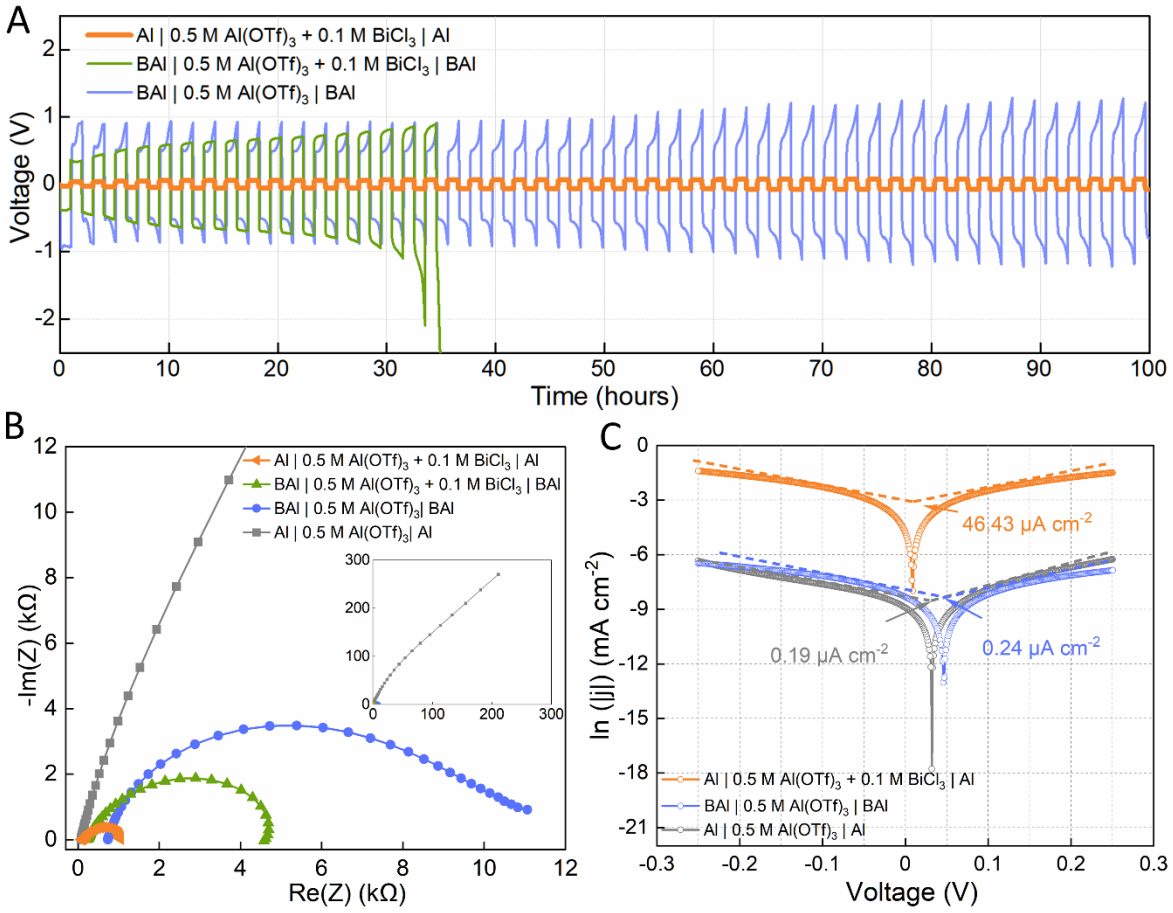

Fig. 3. Electrochemical studies of symmetric cells. (**A**) Comparative plating/stripping study of Al and BAl symmetric cells (at 0.1 mA cm^{-2}, 0.1 mAh cm^{-2}) in different electrolytes. (**B**) Comparative EIS spectra of Al and BAl symmetric cells in different electrolytes; inset shows Fig. 3B zoomed out. (**C**) Tafel curves and corresponding exchange current densities from the linear sweep voltammetry studies (-0.25 V to 0.25 V at 1 mV s^{-1}) of Al and BAl symmetric cells in different electrolytes.

important role of Cl^- is also highlighted here, which for the intrinsic approach can be easily sourced from the anionic part of the $BiCl_3$ present in the electrolyte. We also mention here that the increased current density for the $BiCl_3$ modified electrolyte may have been a result of enhanced corrosion (where we define corrosion as simply the oxidation of the metal anode). However, we reject this possibility of a major corrosion event by using chronoamperometry study presented later as (Fig. S13). We delve deeper into the Tafel study comparing the current-voltage plots of Al | 0.5 M $Al(OTf)_3$ | Al vs. BAl | 0.5 M $Al(OTf)_3$ | BAl (Fig. S6 B provides standard terms and associated concepts used in the discussion below). It can be observed that the exchange current, I_0, and equilibrium potential, E_{eq}, for both the Al | 0.5 M $Al(OTf)_3$ and BAl | 0.5 M $Al(OTf)_3$ is almost the same in the value. This is fundamentally because the expected reaction for both these cases are the same (as the same electrolyte was used in both cases). Of course, the I_0 and E_{eq} values for the case Al | 0.5 M $Al(OTf)_3$ + 0.1 $BiCl_3$ is expected to be different as this electrolyte has been modified, which can lead to a different set of reactions than what is expected in an unmodified electrolyte. Considering the EIS data for Al | 0.5 M $Al(OTf)_3$ | Al vs. BAl | 0.5 M $Al(OTf)_3$ | BAl in Fig. 3B, one can expect that the excessive diffusion polarization happening in the Al | 0.5 M $Al(OTf)_3$ | Al cell should also lead to different values of I_0 and E_{eq} for Al | 0.5 M $Al(OTf)_3$ vs. BAl | 0.5 M $Al(OTf)_3$. However, we note that both these quantities are ascertained based on the reactions at play (i.e., thermodynamics) and not dependent on the polarization (η). Of course, the actual

measured current, j, (what has been plotted in the Fig. 3C) is dependent on the polarization and hence they do not overlap completely for Al and BAl in Fig. 3C.[42]

Combining the results of the EIS and Tafel studies lead us to conclude here that an extrinsic approach can effectively modify the Al surface to reduce ionic resistance, but fails to generate sufficient activity required for plating/stripping. As the intrinsic approach achieves both, it is the preferred approach to be implemented here.

2.4 Anode–electrolyte interfacial study

We conducted a comprehensive study focused on the charge transport characteristics and stability of the intrinsically modified Al-anode interface using EIS and COMSOL simulations. The EIS study was conducted on symmetric Al cells with 0.5 M $Al(OTf)_3$ + 0.1 M $BiCl_3$ electrolyte at rest (Fig. 4A) and during cycling (Fig. 4B). An extremely low impedance ranging from 0.2 kΩ to 1.1 kΩ was observed during rest, indicating an extremely low charge transfer resistance at the interface that is ideal for the plating of Al-ion complex. Over 500 cycles of plating/stripping, this impedance increased to a maximum of 2.1 kΩ, indicating excellent surface properties maintenance. It can be noted here that the EIS spectra here do not show any presence of the Warburg component as also observed in past studies with Mg symmetric cells[43] or Al symmetric cells[13]. This can be because the electron transfer process at the interface might be the rate-determining step, thus dominating the diffusion in the anode bulk or the electrolyte (we demonstrate this point by simulated EIS spectra as shown in Fig. S7 A to D). Thus, the profiles of all EIS spectra collected at regular intervals at both rest and during cycling, indicate a kinetically controlled regime. This suggests that the anode surface is actively controlling the charge transfer at the interface throughout resting and cycling. Here, we point out that maintaining Al anode activity with such low impedance in an RAB for over 500 cycles is exceptional as the Al surface tends to oxidise easily. Temperature-dependent EIS studies were conducted for an intrinsically modified Al surface (Fig. 4C), an unmodified Al surface (Fig. S7E) and an extrinsically modified Al surface (Fig. S7F) to compare surface activation energy (E_a). The temperature dependent EIS spectra were fitted with the respective circuit (insets of Fig. 4C, S7E and S7F) to obtain R_{ct} (total interfacial resistance) values. Here R_{ct} for the circuit in Fig. S7E is the resistance at the Al-electrolyte interface, R_{int}. For the circuit in Fig. 4C or S7B, R_{ct} is the combination of resistance at the Bi-based interphase-electrolyte interface, R_{in}, and the resistance of the bulk Bi-based interphase, $R_{Bi.}$ The reciprocal of R_{ct} is expected to show a temperature-R_{ct} trend that can fit well to an Arrhenius equation as follows:

$$\frac{1}{R_{Ct}} = A\mathrm{e}^{-\frac{E_a}{k_B T}}$$

where Ea is the surface activation energy of ions moving in the surface layer, k_B is the Boltzmann constant, T is the temperature, and A is the proportionality constant [44]. Activation energies calculated from the respective slopes of Arrhenius plot (Fig. 4D) shows least E_a for the Al | 0.5 M $Al(OTf)_3$ + 0.1 M $BiCl_3$ interface, which is negative and significantly lower than that of Al | 0.5 M $Al(OTf)_3$ or BAl | 0.5 M $Al(OTf)_3$. This trend in E_a indicates charge transfer to happen more easily for the intrinsically modified Al. We also note that a negative E_a is rarely observed for charge transfer at the electrode/electrolyte interface, but may be an exception here because of spontaneous reaction between Al and $BiCl_3$. Besides facilitating the diffusion of plating ions, the Bi-based interphase also blocks the drift of electrons across the interphase, as the current-voltage (I-V) characteristics of BAl (Fig. S8) reflect its highly

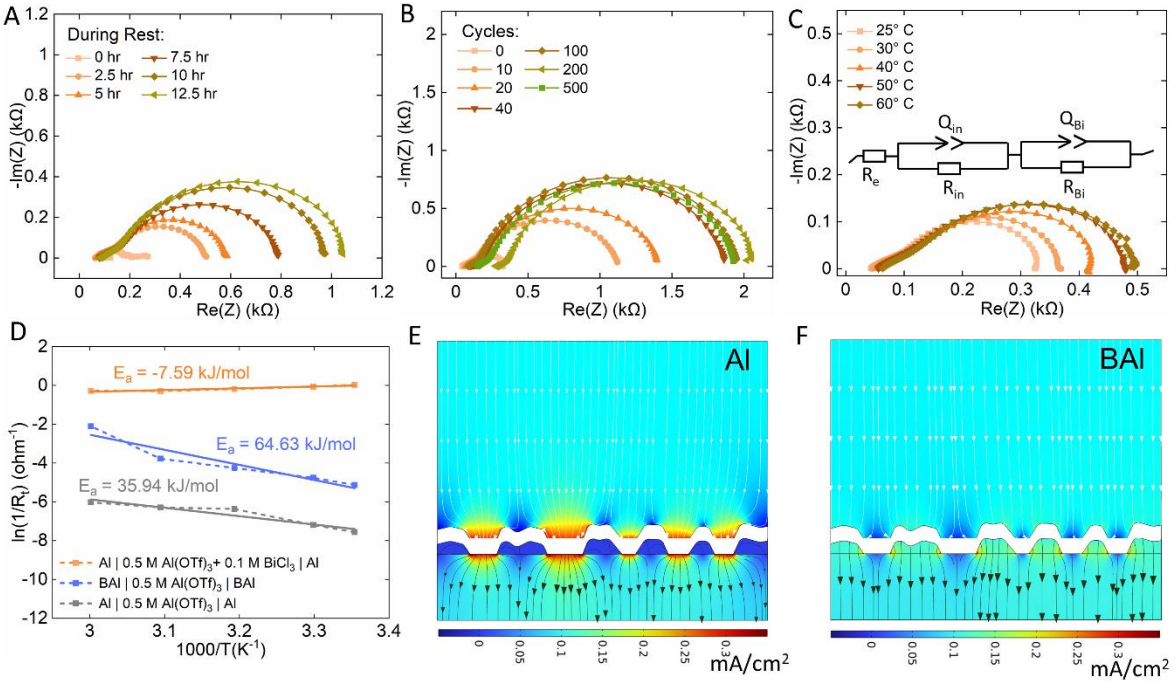

Fig. 4. Anode-electrolyte interfacial study. Nyquist plot collected for Al symmetric cell in 0.5 M $Al(OTf)_3$ + 0.1 M $BiCl_3$ electrolyte (**A**) at every 2.5 hrs interval after fabrication, (**B**) at different cycling stages of plating/stripping and (**C**) at varying temperatures (inset: circuit used for fitting spectra in Fig 3 C; R_e – Electrolyte bulk resistance, R_{in} – Bi based interphase/electrolyte interfacial resistance, R_{Bi} – Bi-based interphase bulk resistance. Q_{in} – Bi-based interphase/electrolyte interfacial capacitance, Q_{Bi} – Bi-based interphase bulk capacitance). (**D**) Arrhenius plot of reciprocal of charge transfer resistance (obtained after fitting respective data in Fig 3C, Fig. S7E and Fig. S7F) versus the inverse of the temperature with the respective derived activation energies from the slopes. COMSOL simulations (at 0.1 mA cm^{-2}) derived current density distribution at the electrode-electrolyte interface of (**E**) Al and (**F**) BAl.

resistive behavior compared to the Al metal. We mention here that an electronically insulating SEI layer, as demonstrated by the resistive behavior of the Bi based artificial layer, is important here as it can prevent persistently parasitic reactions between the anode and the electrolyte by blocking the electron transport[45].

To compare the dynamic behavior of the Al anode vs. the Bi-protected Al anode surfaces during the Al-ion complex deposition process, a finite element method (FEM) was used to investigate the electrical field distribution and material flux distribution at the anode-electrolyte interphase through a COMSOL simulation. Both the systems were modeled as 2D geometries with a rugged anode surface as observed from the respective SEM micrographs (Fig. 2A and B). The rugged morphology was used as it also mimics a more realistic deposition process in which some material may be deposited after the formation of islands on the surface. Both the models differed from each other in terms of surface ionic conductivity, with the conductivity of the Al surface one fourth that of protected Al (this is based on the total impedance of Al vs BAl surfaces from Fig. S7). Current densities derived from the COMSOL simulations for the Al (Fig. 4E) and BAl (Fig. 4F), show contrasting distributions at the interface. For the Al surface, a higher current density was observed in the valleys formed by the protruding rough surfaces. Not only that, but the current density distribution was also wider, varying from 0 to 0.35 mA cm^{-2}. However, lower current densities were observed in the valley area for the BAl surface, along with a much narrower current density

distribution (0–0.2 mA cm^{-2}). This contrast became clearer when comparing the current density distribution of Al vs. BAl at higher rates of 1 mA cm^{-2} and 5 mA cm^{-2} (Fig. S9). As compared to the Al interface, the BAl interface showed lower current densities and narrower current distributions even at higher rates. A narrower current distribution is preferred as it increases the possibility of uniform material flux. This leads to uniform metal plating and avoids the possibilities of dendrite formation.[46] This observation is supported when comparing the materials flux distribution at the Al and BAl interface for different current densities (Fig. S10) in which a narrower distribution of Al-ion is seen across the BAl-electrolyte interface. Our results show the Bi-protected surface to be more capable of regulating and guiding uniform deposition.

2.5 The unique additive-salt combination

Here we investigated the evolution of Al-ion complexation as a result of $BiCl_3$ introduction in the 0.5 M $Al(OTf)_3$/DME electrolyte and present the results of corrosion study and comparative cost analysis of our optimized electrolyte. MD simulation study has been used to understand the trends in the evolution of Al-ion solvation sheath, which are further verified by the electrolyte speciation study done by Raman spectroscopy.

Utilizing MD simulations, we computed the distribution of ion/molecules around the Al-ion in three electrolyte systems with differing amounts of $BiCl_3$, i.e 0.5 M $Al(OTf)_3$, 0.5 M $Al(OTf)_3$ + 0.05 M $BiCl_3$ and 0.5 M $Al(OTf)_3$ + 0.1 M $BiCl_3$ (Fig. S11 A). The evolution of

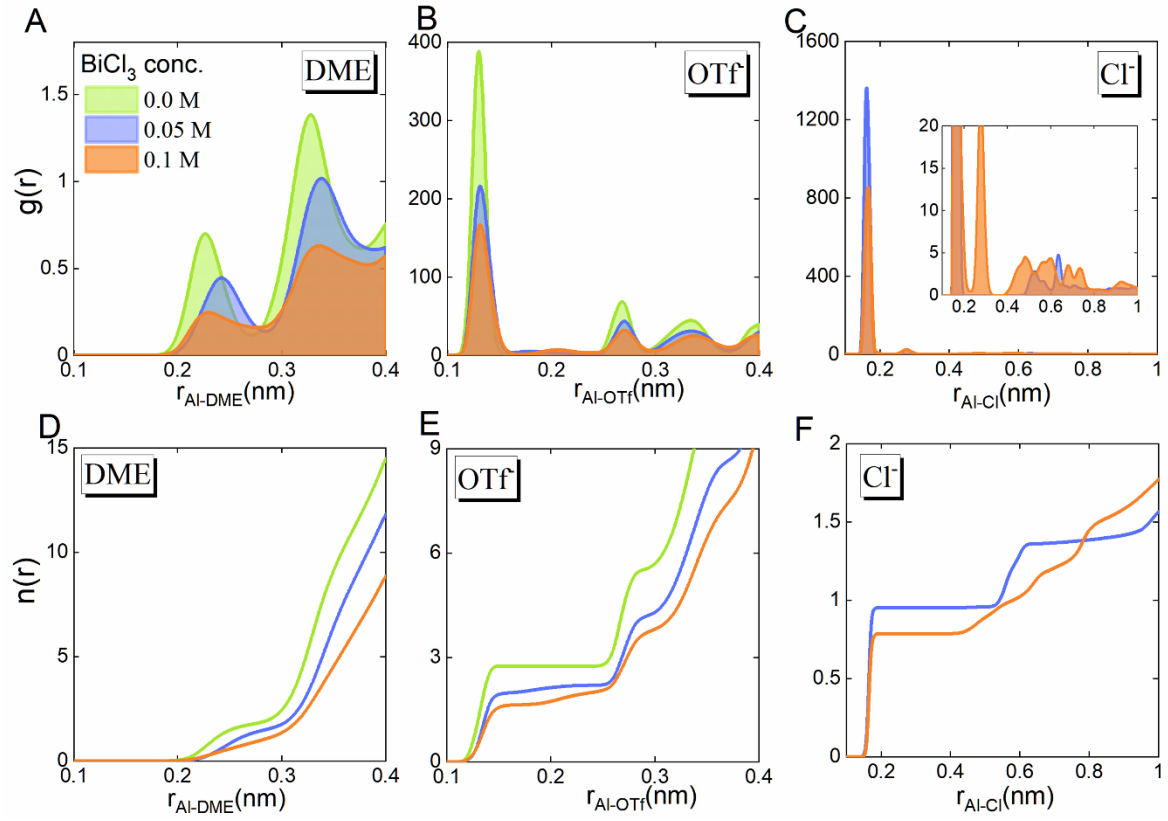

Fig. 5. Molecular dynamics-based electrolyte solvation study. Radial distribution function (RDF), g(r), of (**A**) DME, the solvent, (**B**) OTf^- and (**C**) Cl^- as a function of radial distance (r) from Al^{3+} ion for the three electrolyte systems – 0.5 M $Al(OTf)_3$, 0.5 M $Al(OTf)_3$ + 0.05 M $BiCl_3$ and 0.5 M $Al(OTf)_3$ + 0.1 M $BiCl_3$. Running coordination number of (**D**) DME, (**E**) OTf^- and (**F**) Cl^- corresponding to figures (A), (B) and (C) respectively.

Al-ion solvation sheath is shown by the radial distribution functions (Fig. 5A-C) and the corresponding coordination number (Fig. 5D-F) of DME, OTf^- and Cl^- are plotted against their radial distances from the Al-ion. Up to a radial distance of 0.4 nm, DME molecules are observed to be mainly present in two solvation sheaths at ~0.22 nm and 0.32 nm (Fig. 5A). A clear decline in the density of DME molecules within such solvation sheath was observed with an increasing amount of $BiCl_3$, which is also reflected in the reduction of Al-DME co-ordination number (Fig. 5D). Similarly, OTf^- molecules were observed to be mainly concentrated in the solvation sheath at ~ 0.13 nm from the Al-ion and their density decreased linearly with the increase in $BiCl_3$ concentration (Fig. 5B). The corresponding Al-OTf^- coordination number also decreased from ~2.7 to ~1.7 when the $BiCl_3$ concentration was increased to 0.1 M (Fig. 5E). A reduced amount of OTf^- around Al-ion indicates possibility of more free OTf^- ions in the electrolyte, which might aid in the formation of SEI layer [11]. The density distribution of Cl^- ions are concentrated mainly in solvation sheath at 0.16 nm and increased when 0.05 M $BiCl_3$ was added to the 0.5 M $Al(OTf)_3$ electrolyte (Fig 5C). However, very surprisingly, the Cl^- ion density in the first solvation sheath decreased when the concentration of $BiCl_3$ was increased further to 0.1 M. The reason for these increasing and decreasing trends becomes clear after the Raman analysis as done below. The presence of Bi is mainly detected after 0.4 nm from the Al-ion (Fig. S11 B and C), which is expected because of positive-positive charge repulsion between Al and Bi ions.

The results of Raman analysis (Fig. 6A) verified successful Al-Cl complexation in 0.1 M $BiCl_3$ + 0.5 M $Al(OTf)_3$ electrolyte and confirmed the trends observed from the MD simulation. The Raman data of the $Al(OTf)_3$ electrolyte shows the characteristic OTf^- peaks at 350 cm^{-1}, 777 cm^{-1} and 1069 cm^{-1}, corresponding to $\delta_{asym}SO_3$ and δ_{asym} CF_3, $\nu_{sym}CF_3$ and ν_{sym}C-S, and ν_{sym} CS signals, respectively [31]. Peaks at 777 cm^{-1} and 1069 cm^{-1} showed red shifts upon dissolution in the electrolyte, indicating a change in their respective complexation. Most interestingly, with the increasing amount of $BiCl_3$ in the electrolyte, two peaks appeared at 307 $cm^{-1}$and 354 cm^{-1}. These peaks correspond to $Al_2Cl_7^-$ and $AlCl_4^-$ respectively [11, 47]. With an additive concentration increased to 0.1 M and further in the electrolyte, the peak corresponding to $Al_2Cl_7^-$ showed a much stronger signal relative to the $AlCl_4^-$ peak, indicating that at higher concentrations of additive, the $Al_2Cl_7^-$ species might predominate. We note here that the dominant presence of $Al_2Cl_7^-$ results in a quantitative reduction in Al-Cl complexation as Cl^- ion per Al^{3+} is 3.5 and 4 for $Al_2Cl_7^-$ and $AlCl_4^-$ respectively. This explains the increasing and then decreasing Al-Cl complexation trend that was observed from the MD simulations with the increasing concentration of $BiCl_3$ additive in the electrolyte. We speculate that the relative concentration of $Al_2Cl_7^-$ and $AlCl_4^-$ may play a role in determining the plating/stripping behavior [48], but could not determine the exact nature of this role here. Additional Raman analysis of varying concentrations of $BiCl_3$ in 0.1 M $Al(OTf)_3$ (Fig. S12) showed the absence of $Al_2Cl_7^-$ and $AlCl_4^-$ species, indicating that Al-Cl complexation may not happen in all the cases of $BiCl_3$ being added to $Al(OTf)_3$.

Combining the MD results and Raman analysis, we find that adding 0.1 M $BiCl_3$ to 0.5 M of $Al(OTf)_3$ results in successful Al-Cl complexation (Fig. 6B), which is realized by the presence of $Al_2Cl_7^-$ and $AlCl_4^-$. The detection of these species is critical for a RAB system as they are conventionally known to be the charge-carrying species in the electrolyte [11, 47]. $Al_2Cl_7^-$ is known to reduce at the anode to deposit Al, while $AlCl_4^-$ is known to oxidize at the cathode by intercalation, thus completing the charge carrying loop in the electrolyte [11, 47].

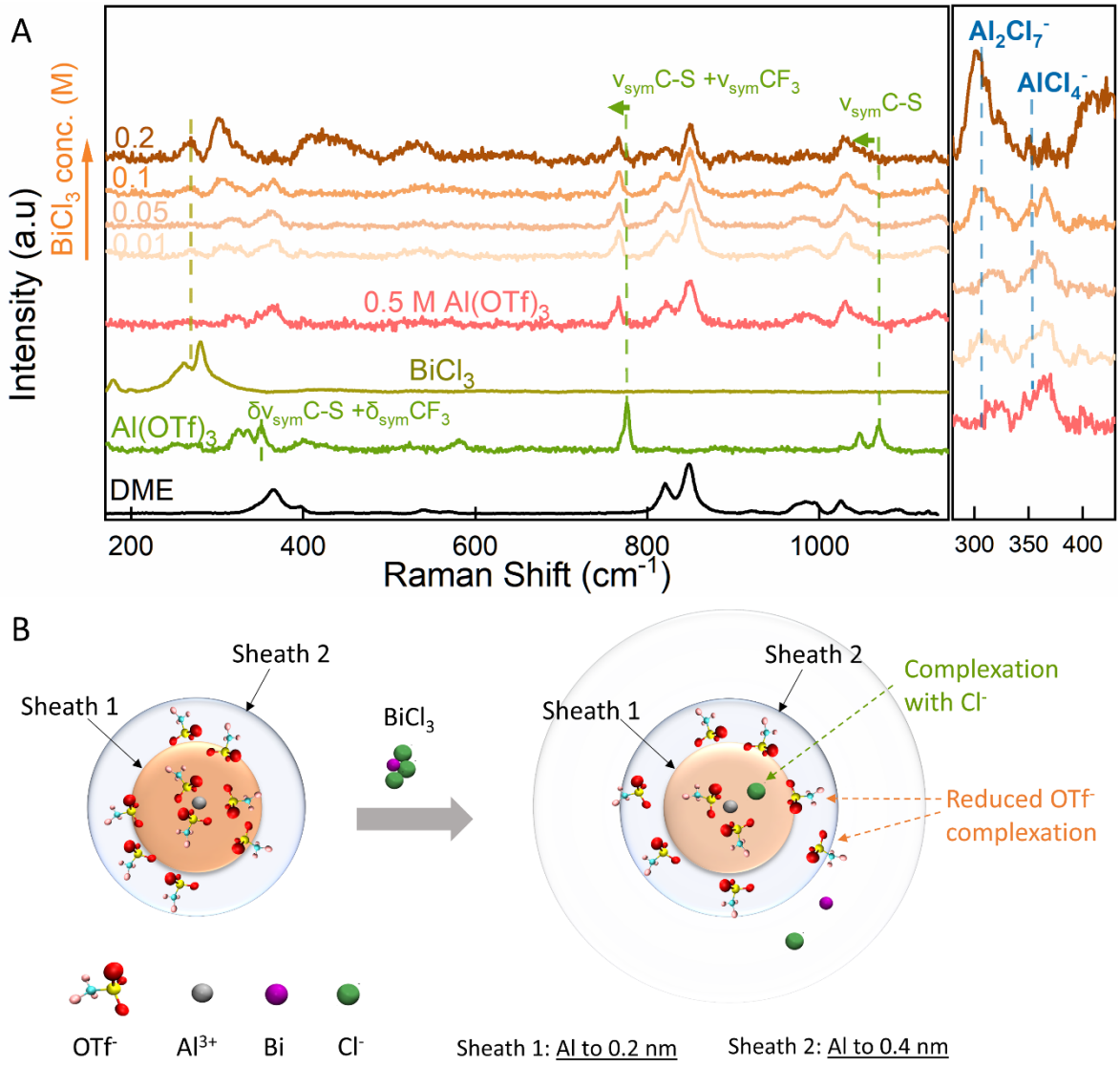

Fig. 6. Electrolyte speciation study. (**A**) Raman spectra obtained for DME, $Al(OTf)_3$, $BiCl_3$ and varying concentrations of $BiCl_3$ in 0.5 M $Al(OTf)_3$. (**B**) Schematic illustration of evolution in the solvation sheath around Al-ion upon introduction of $BiCl_3$ in the electrolyte.

We further carried out a comparative corrosion study of our optimized electrolyte with commercial $AlCl_3$ + EMICl (3:2) to demonstrate its reduced corrosive nature. Chronoamperometry experiments conducted on Ti, stainless steel (SS), Ni, and Mo electrodes (Fig. S13) show significantly reduced corrosion in the $BiCl_3$-modulated electrolyte. When subjected to potentials ranging from 1 V to 2.6 V, Ti, SS, and Ni exhibited a lower leakage current in our electrolyte compared to the $AlCl_3$ + EMICl electrolyte. In the latter case, both SS (Fig. S13B) and Ni (Fig. S13C) showed a sharp increase in leakage current (~10 mA cm^{-2}) when the voltage reached 1.5 V, while the leakage current for Mo remained low in both electrolytes. These findings from the chronoamperometry studies indicate suppressed side reactions and substantially reduced corrosion in $BiCl_3$-based electrolyte, as compared to the traditional $AlCl_3$ + EMICl electrolyte. Moreover, a price comparison shows the $BiCl_3$-based electrolyte to be approximately five times more affordable than the conventional $AlCl_3$ + EMICl eutectic electrolyte, and about four times more economical than the $AlCl_3$ + urea eutectic analogue electrolyte (Table S1). The main source of price reduction comes from the eliminating the use of anhydrous $AlCl_3$, which is moisture sensitive and corrosive.

2.6 Mechanism of plating/stripping

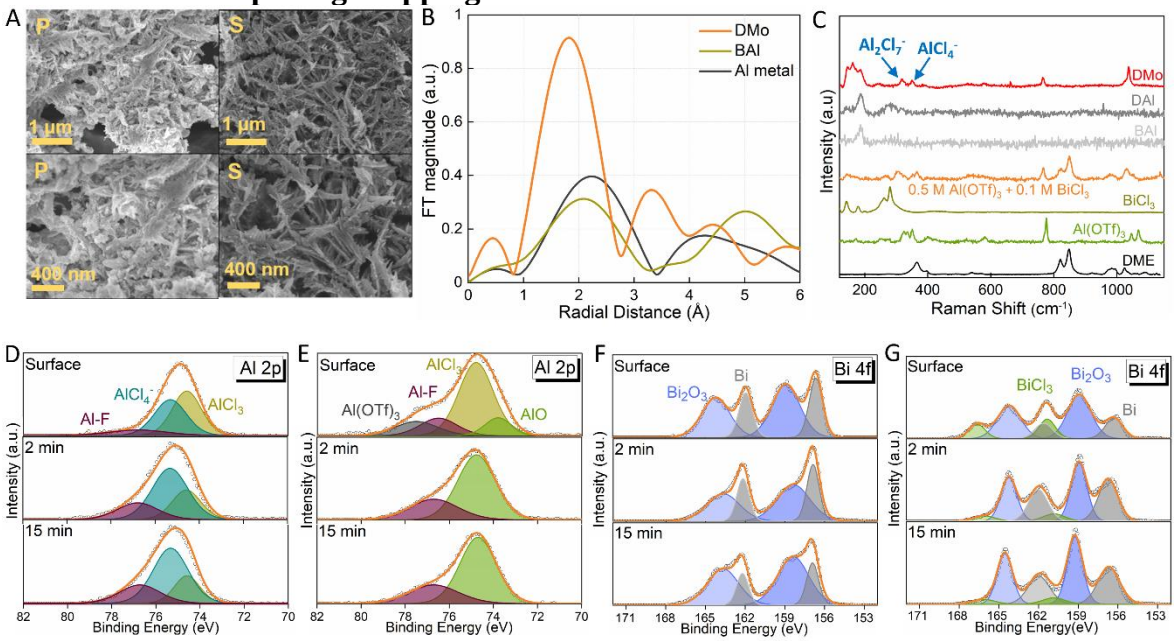

Fig. 7. Mechanism of Al deposition through the artificial interphase-protected Al. (**A**) SEM image of plated, P, and stripped, S, electrode at two different magnifications, obtained from Al | 0.5 M $Al(OTf)_3$ + 0.1 M $BiCl_3$ | Al cell after 24 cycles of plating/stripping. (**B**) Fourier transformed EXAFS spectra (uncorrected for the phase shift) derived from the Al K-edge obtained for DMo, BAl, and Al metal. (**C**) Raman spectra obtained for DMo, DAl, BAl and standards including 0.5 M $Al(OTf)_3$ + 0.1 M $BiCl_3$ electrolyte, DME, $Al(OTf)_3$ and $BiCl_3$. Al 2p (**D**), (**E**) and Bi 4f (**F**), (**G**) region of XPS spectra for the surface and etched layers (2 min and 15 min) of plated, (D) and (F), and stripped, (E) and (G), electrodes.

In this section, we elucidate the mechanism of plating/stripping using a combination of characterization techniques on complementary materials. SEM micrographs showed contrasting material volume on the plated vs. stripped samples (Fig. 7A), with the plated electrode being denser than the stripped electrode. A side-to-side comparison of plated and stripped samples with pristine Al and BAl (Fig. S14) provide insight into developing surface morphology on the Al anode. As already discussed, upon reaction with $BiCl_3$, the surface of Al anode becomes textured. Upon plating, this textured coating becomes denser and more uniform, likely because of plating of Al metal and the presence of $AlCl_4^-$. Further, upon stripping, the surface morphology becomes hollow, with the textured remnants of Bi and possibly SEI layer. EXAFS analysis further revealed the local geometric structure of the plated Al complex (Fig. 7B). For the DMo sample, a high intensity peak corresponding to the first shell co-ordination was observed at ~ 2 Å. This peak's higher intensity as compared to that of metallic Al indicates that the plated species is either coordinated by a larger number of atoms or by denser atoms as compared to coordination around metallic Al. Thus, we have proof of a deposition process happening that differs from Al^{3+} reducing to form metallic Al. The intensity difference in the first shell co-ordination peak of DMo vs BAl revealed the reaction between Al and $BiCl_3$ to not have formed the plating species.

Further, Raman analysis of DMo sample (Fig. 7C) show the presence of $AlCl_4^-$ and $Al_2Cl_7^-$, which were not observed when Al was reacted either with $BiCl_3$ (BAl) or with the Bi modulated electrolyte (DAl). The Al 2p region of the XPS spectra for the plated sample (Fig. 7D) revealed the presence of $AlCl_4^-$ [49], $AlCl_3$ [35] and Al-F [35] on the surface and even after etching for 15 mins. Conversely, the stripped electrode did not have $AlCl_4^-$ present, but had

Al-F detected throughout and $AlCl_3$ found majorly on the surface (Fig. 7E). The 2 min and 15 min sample's spectra (in Fig. 7E) were not deconvoluted with $AlCl_3$ peak because very less metallic Cl^- was detected corresponding to them (Fig. S15A). The Bi 4f region of the XPS spectra for the plated sample (Fig. 7F) revealed the presence of only Bi and Bi_2O_3 throughout the etched layers [34]. On the other hand, the Bi 4f region of XPS spectra for the stripped sample showed the additional presence of $BiCl_3$ (Fig. 7G). Concluding from the XAS, Raman and XPS analyses, we propose the following reaction mechanism of plating on the Al surface. $Al_2Cl_7^-$ from the electrolyte reduces on the Bi-modified Al anode surface to form $AlCl_4^-$ and Al (equation 1). At the same time, this newly formed Al partially deposits on the Al substrate and partially reacts with unreacted $BiCl_3$ to generate $AlCl_3$ (equation 2) as detected in the plated sample. Upon stripping, $AlCl_4^-$ consumes metallic Al to form $Al_2Cl_7^-$, which also drives equation 2 in the reverse direction, causing $BiCl_3$ to reappear and $AlCl_3$ to diminish in the stripped sample.

Plating at the anode:

$$4Al_2Cl_7^- + 3e^- \rightleftharpoons Al + 7AlCl_4^- \qquad Equation\ 1$$

$$Al + BiCl_3 \rightleftharpoons AlCl_3 + Bi \qquad Equation\ 2$$

2.7 Material distribution on the anode

Here we investigated the distribution of material on the cycled electrodes using time-of-flight secondary ion mass spectrometry (TOF-SIMS) in which the 3D reconstructions of the sputtered volume for the plated and stripped electrodes allows us to understand the formation of multi-layered interphases on the Al anode and the precise location of Al-ion complex reduction during plating. Notably, the sputtering depths differed for negative and positive ion fragments, as indicated by the accompanying scale on the 3D maps (Fig. 8). Both plated and stripped electrodes exhibited a thin layer comprising of a Bi-based compound (Fig. 8A) that remains primarily distributed on the top surface. These Bi-based compounds are likely to be metallic Bi and Bi_2O_3 as ascertained in the XPS study.

Furthermore, F and S based compounds were detected up to a depth of 0.8 μm in the bulk material (Fig. 8B). These species were present in both plated and stripped samples, with F likely corresponding to metallic fluoride (Al-F), as observed in the XPS analysis. Although the identity of S could not be definitively determined, it was found in relatively small amounts. The distribution of Cl^- showed distinct variations between the plated and stripped samples (Fig. 8C). The plated sample exhibited a higher concentration of Cl-based compounds primarily concentrated in the upper layer of the electrode. Furthermore, mapping of Al-Cl^+ in Fig. 8C indicated its higher presence in the plated sample, with a relatively uniform distribution throughout the bulk. This observation suggests that haloaluminated species penetrated through the top surface interphases, with subsequent reduction at the bulk of the Al metal - protective interphase interface. Additionally, a 2D reconstruction of Al_2^+ in Fig. 8D provides clear evidence of Al plating, as evidenced by the relatively higher intensity in the plated sample. Based on the depth where ion-fragments are found, we reconstructed the material distribution in the cycled Al electrode (Fig. 8E) and conclude that: (i) the bilayer interphase consisting primarily of Bi-based compounds on the top surface and F- and S-based compounds immediately beneath it is present on the Al anode throughout the cycling process and (ii) the plating process on the anode involving the reduction of $Al_2Cl_7^-$ to form $AlCl_4^-$ and Al occurs directly beneath the aforementioned bilayer interphase.

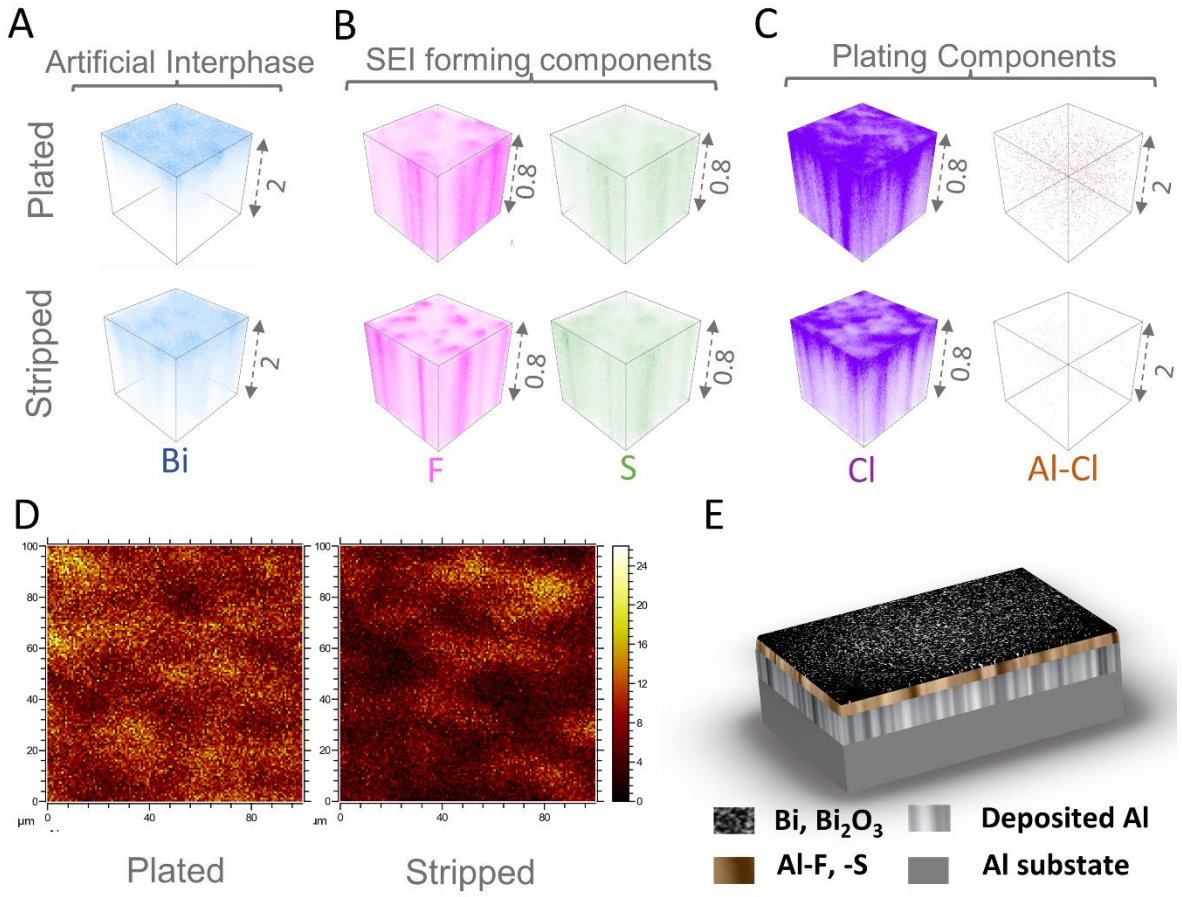

Fig. 8. Material distribution in the cycled electrode. TOF-SIMS derived 3D reconstruction of the sputtered volume of several secondary ion fragments for the plated and stripped samples (with sputtering depth indicated in µm): (**A**) Bi^+, (**B**) F^- and S^-, (**C**) Cl^- and $Al\text{-}Cl^+$, (**D**) 2D reconstruction of the sputtered volume of Al_2^+ for the plated and stripped samples. (**E**) Schematic 3D illustration of the cycled electrode.

2.8 Electrochemical performance of Bi-protected Al

Here we demonstrate long-term symmetric and asymmetric cell performance. A long-term Al symmetric cell plating/stripping study with 0.1 M $BiCl_3$ + 0.5 M $Al(OTf)_3$ shows an unprecedented low overpotential of <0.1 V sustained for 4000 hrs (Fig. 9A). To the best of our knowledge, this is: (i) the lowest overpotential achieved in a non-$AlCl_3$ based electrolyte and is comparable with the plating/stripping overpotential in $AlCl_3$-based electrolytes (whether eutectic, gel or high temperature types; Fig. 9B derived from Table S6) and (ii) the longest cycling life reported for any RAB anode, irrespective of the presence of $AlCl_3$ (Table S6 and Fig. 9B). We also note that our anode-electrolyte combination shows an adequately low overpotential at higher rates of plating/stripping ranging from 0.1 to 0.5 mA cm^{-2} (Fig. S15 B). An asymmetric cell study, conducted in a 3-electrode flooded cell setup with Mo as working electrode and Al as reference and counter electrodes (Fig. 9C) demonstrates the practical use-case of our electrolyte. Sharper plating/stripping curves were observed with cycling, which is indicative of suppressed side reactions. Calculations of cycling Coulombic efficiency showed a gradual improvement from 92.8% to 95.3% over 50 cycles (see Fig. 9C inset) which is also reflected by the reduced side reactions at the end of the stripping step (as marked by the black area in Fig. 9C inset).

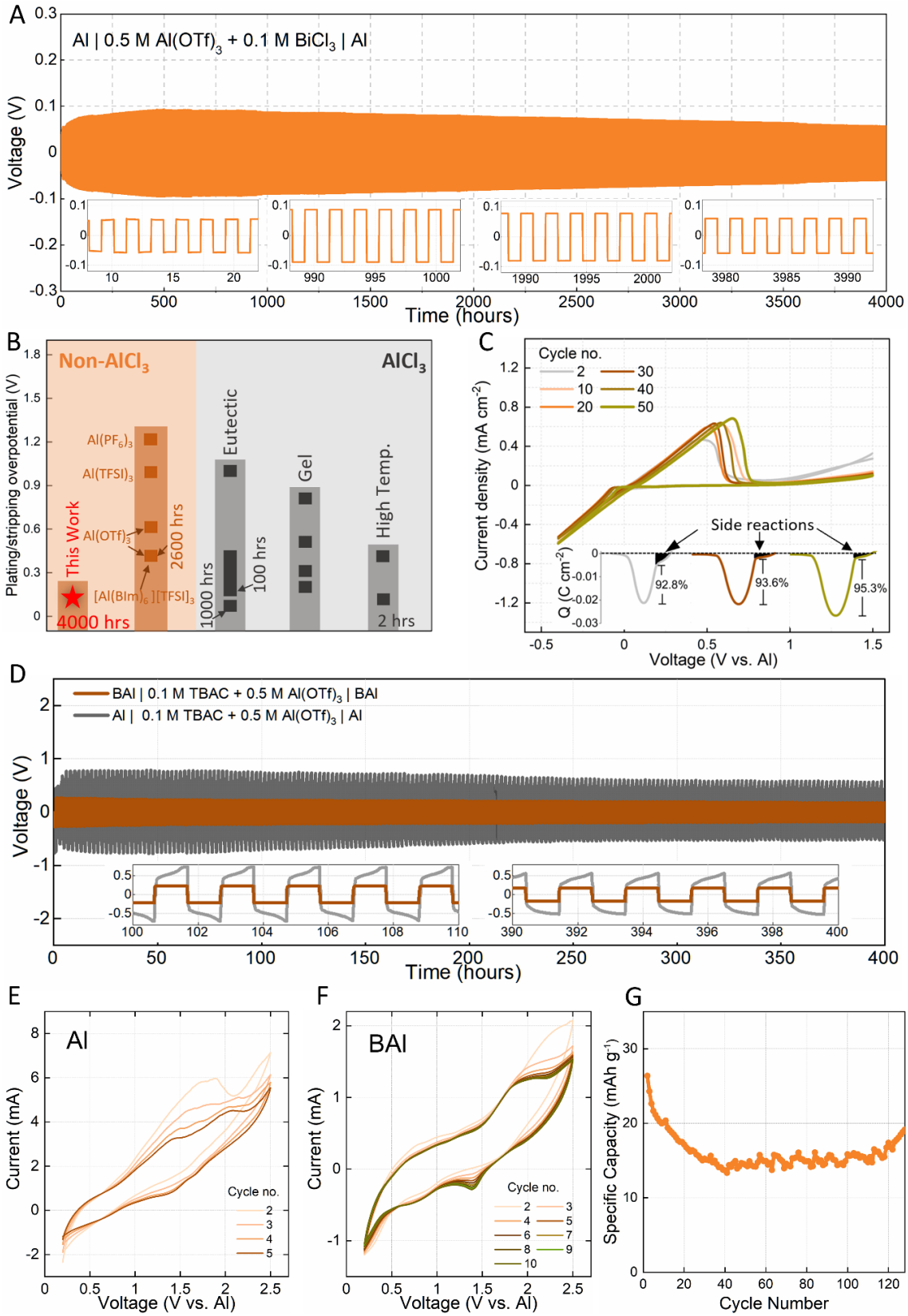

Fig. 9. Cell performance and benchmarking. (**A**) Long term plating/stripping study of Al symmetric cell in 0.5 M $Al(OTf)_3$ + 0.1 M $BiCl_3$ at 0.1 mA cm^{-2} and 0.1 mAh cm^{-2}. (**B**) Anodic overpotential and plating/stripping cycling life (shown in hrs) comparison of our work (red star) with the non-$AlCl_3$ (orange squares) and $AlCl_3$-based (grey squares) organic electrolytes reported for RAB (See Table S6 for details). (**C**) CV scan at 10 mV s^{-1} in 0.5 M $Al(OTf)_3$ + 0.1 M $BiCl_3$ electrolyte with Mo as working electrode, and Al as counter and

pseudo reference electrode (inset shows coulombic efficiencies for the 2nd, 30th and 50th cycles). (**D**) Comparative plating/stripping study of Al and BAl symmetric cells (at 0.1 mA cm^{-2}, 0.1 mAh cm^{-2}) in TBAC modulated electrolyte. CV scan (at 10 mV s^{-1}) of $FeVO_4$ full cell in 0.5 M $Al(OTf)_3$ + 0.1 M TBAC with (**E**) Al anode and (**F**) BAl anode. (**G**) Cycling stability study for the $FeVO_4$ - BAl full cell in 0.5 M $Al(OTf)_3$ + 0.1 M TBAC at 100 mA g^{-1}.

In addition, we demonstrate the possibility of using an extrinsically Bi-coated Al anode by testing it in a TBAC-modulated 0.5 M $Al(OTf)_3$ electrolyte. Plating/stripping comparison of Al vs BAl symmetric cells in a TBAC-modulated electrolyte (Fig. 9D) indicates the overpotential for the BAl system to be half that of the Al system. This reduction of overpotential to ~ 0.2 V can be sustained over 400 cycles, suggesting that an extrinsically Bi-coated anode is better than a bare Al anode. The advantage of using Bi-protected Al anode is also reflected from the full-cell study. A $FeVO_4$ cathode when cycled with bare Al anode fails to show cathodic peaks corresponding to the intercalation/deintercalation of Al-ion/Al-ion complexes, likely $AlCl_4^-$ here (Fig. 9E).[24] The cathodic current during the negative scan remains substantially low and the voltammogram is unstable, indicating non-recurring reactions over repeated cycling. But when the same $FeVO_4$ is cycled alongside Bi-protected Al, well defined cathodic peak appears (Fig. 9F) in overlapping cyclic voltammograms generated over repeated cycling. We co-relate the appearance of cathodic peak to the enhanced anodic activity of Al when it is protected by Bi. We had observed in Fig. 1B that Al stripping happens only when Bi is providing protection to Al anode, whereas, in the non-modulated 0.5 M $Al(OTf)_3$, stripping does not occur. Failure to strip Al in $FeVO_4$ | Al full cell implies the unavailability of ions from the anode side to replenish the electrolyte, hence, the suppressed cathodic peak of $FeVO_4$. Conversely, during the discharge of the $FeVO_4$ | BAl full cell, Al is stripped off the anode releasing $Al_2Cl_7^-$ ions in the electrolyte and electrons in the outer circuit which are subsequently absorbed at the cathode to release $AlCl_4^-$ in the electrolyte. Hence the charge circuit gets completed and the consequent observance of cathodic peak for $FeVO_4$. A discharge capacity of 20 mAh g^{-1} could be sustained for 128 cycles at 100 mA g^{-1} (Fig. 9G and S16), which is subject to further performance improvements. It can also be noted here than in a 0.5 M $Al(OTf)_3$ + 0.1 M $BiCl_3$ electrolyte with Al anode, it might not be possible to run a full-cell as demonstrated by the completely failed CV in Fig. S16 B. We speculate that this can be because of the reaction between Bi and cathode, and subsequent blockage of cathode surface for the reaction.

Finally, we apply our general design strategy in a non-Al battery system. When cycling a magnesium symmetric cell in a 0.5 M $Mg(OTf)_2$ electrolyte versus a 0.5 M $Mg(OTf)_2$ + 0.1 M $BiCl_3$ electrolyte, a remarkable tenfold reduction in the plating/stripping overpotential is observed, decreasing from 3 V to approximately 0.3 V (Fig. S17). Notably, this low overpotential is sustained for over 500 hours, suggesting the formation of a stable interface on the Mg metal surface that protected it from unwanted side reactions such as oxidation.

3. Conclusion

Our study investigated a series of metal chloride additives and identified $BiCl_3$ as the ideal additive for $Al(OTf)_3$ electrolyte in RAB systems. $BiCl_3$ is demonstrated to be an exceptionally effective additive as both its cationic and anionic parts enable critical battery functionality. $BiCl_3$ reacts in situ with the Al anode surface via an ion exchange reaction and donates its cationic part to form a Bi-rich protective interphase on the anode. This interphase protects the Al anode from severe oxidation and maintains its activity over repeated cycling. The interphase also enables low surface activation energy and high ionic conductivity at the anode-electrolyte interface, producing an extremely low overpotential of plating/stripping. The anionic part of $BiCl_3$ generates $Al_2Cl_7^-$ in the electrolyte, which reduces reversibly at the

Al anode to plate Al metal. Protecting the Al metal and generating electroactive species are both equally critical in achieving a sustained low overpotential of plating/stripping, which is made possible here with an intrinsic method of forming an artificial interphase. This study demonstrates the significance of not only selecting the chloride salt of Bi as an additive, but also considers the strategy of developing the protective interphase on a case-by-case basis. Our detailed investigation of the reaction mechanism and material distribution at the anode verifies the superior performance of our $BiCl_3$-modulated electrolyte-anode system. Low corrosion and pricing also make this electrolyte commercially attractive. We believe that this study notably advances anodic performance in RAB systems and its results can be applied to other metal battery systems such as magnesium-ion batteries.

4. Materials and Methods

4.1 Preparation of Al-anode

High purity Al foil (0.1 mm (0.004 in) thick, 99.99% (metals basis), CAS: 7429-90-5) was dried overnight in an oven (80 °C) and transferred to an argon filled glovebox (O_2 < 1.2 ppm and H_2O < 0.1 ppm). These foils were punched out in the form of circular disks, polished with sandpaper of grit size 1000 or 2000 and then used in a battery cell as the anode. For the extrinsically coated anodes (i.e. BAl), the polished Al foils were first dipped in the 0.1 M $BiCl_3$/DME solution for 10 mins, and then rinsed in DME solvent to remove excessive Bi or $BiCl_3$ before use. We note here that, even though the glovebox is a low-concentration O_2 environment, it is important that Al foil is polished freshly either before coating or when using it directly as anode in the cell. This avoids the thin native oxide layer forming on the Al anode to allow sufficient and uniform reaction of Al with $BiCl_3$. Sample DAl was prepared by exposing polished Al to 100 µl of 0.5 M $Al(OTf)_3$ + 0.1 M $BiCl_3$; DMo was prepared by plating polished Mo foil in a 3 electrode setup for 2 hrs at 0.5 mA cm^{-2} in 0.5 M $Al(OTf)_3$ + 0.1 M $BiCl_3$.

4.2 Cell fabrication

The cells were fabricated inside the glovebox either in a 2032-coin cell or 3 electrode flooded beaker setup. Coin cells were assembled with appropriate electrodes and 80 µl of electrolyte soaked on the glass fibre separator (WhatmanTM, GF/A; dried at 150 °C for at least 4 hours). Three-electrode cells with working (WE), counter (CE) and reference electrodes (RE) dipped in a beaker flooded with electrolyte were used for the corrosion and asymmetric cell study. For the corrosion study, one of stainless steel, Ni, Ti or Mo was used as the WE with polished Al as the RE and CE. Pt, Ti and Mo as the WE with Al as the RE and CE were used for the asymmetric cell study. Mg symmetric cells were prepared similarly to the Al symmetric cells. $FeVO_4$ was synthesized by the same methodology as in [9]. $FeVO_4$ was mixed with acetylene black and dissolved in a PVDF binder/NMP solution in 7:2:1 weight ratio of active material to acetylene black to PVDF. This slurry was stirred overnight and coated on carbon paper to be used a cathodes in full cell study.

4.3 Electrochemical characterization

The cells were allowed to rest for at least 5 hours after fabrication before electrochemical characterizations were conducted (except for the EIS study during rest). The measurements were performed using either a Gamry 3000 or Gamry 1010 potentiostat for CV and EIS studies. CV for the plating/stripping study was conducted using a 3-electrode setup. In EIS measurements, a total of 10 frequency points were logarithmically distributed per decade in the frequency range of 100 kHz to 0.01 Hz with a voltage amplitude of 5 mV. Temperature-dependent EIS studies were performed in a temperature-controlled chamber at temperatures

from 25 °C to 60 °C. We used the Neware Battery Testing System (BTS) to conduct plating/stripping studies in a coin cell.

4.4 Materials characterization

A 785-nm argon laser (Renishaw Invia Confocal) was used for the Raman spectroscopy of all samples, including powder salts, solvent, electrolyte, and electrodes. FESEM was conducted using JEOL 7600F operated at 5 keV to collect micrographs of the Al anode. EDX signals were also captured using JEOL 7600F operated at 15 keV. Kratos Axis Supra+ equipped with 1486.69 eV, Al K_α radiation was used to collect XPS signals. XPS depth profiling was conducted using a 700 μm x 300 μm beam size scanning over a sputtered area of 2 mm x 2 mm raster. A 5 keV Ar cloud sputtering with estimated etch rate of 3.125 nm/min (based on SiO_2) was used. For the narrow scan, pass energy of 20 eV with a step size of 0.1 eV was used. For the survey spectrum, pass energy of 160 eV with a step size of 1 eV was used. The process of peak deconvolution was carried out using CASA XPS software. Shirley background subtraction was applied, and a model peak consisting of a combination of Lorentzian and Gaussian distributions (in a ratio of 30:70) was utilized. The calibration of all the data was performed at 284.8 eV due to the presence of adventitious carbon. XRD patterns were measured on an X-ray diffractometer (D8 Advance, Bruker) with Cu-Kα radiation under 40 kV and 40 mA. For the depth profiling, a TOF.SIMS 5 (ION-TOF GmbH, Germany) instrument was employed with a pulsed Bi_1^+ primary ion beam (13.3 ns pulse width, 30 keV energy, 3 pA current) and a Cs^+ sputtering ion beam (2 keV energy, 56 nA current). During the depth profiling, the primary analysis beam was scanned over an area of 100 μm × 100 μm that was centered within the regressing Cs^+ sputtered area (300 μm × 300 μm). The profile was acquired in interlaced mode, i.e., the analysis was performed while the Cs^+ beam was sputtering the sample surface. All detected ions had either negative or positive polarity while the mass resolution was >3600 (m/δm) for all detected secondary ion fragments of interest. The data were acquired at a base pressure of 3.6×10^{-8} Torr. A constant current electron beam (20 eV energy, 9 μA current) was directed onto the sample during depth profiling to reduce the sample charging. XAS measurements were carried out for the Al K-edge at the Beamline 8, Synchrotron Light Research Institute (SLRI), Thailand, in fluorescence mode. The electron energy was 1.2 GeV, beam current 150 - 50 mA, and the maximum photon flux was about 8.0 x 10^9 photons/s/100mA. KTP (011) double crystals were utilized as a monochromator. The background subtraction was done using the Athena program.

4.5 Simulation methodology

MD simulation: All of the MD simulations were performed using GROMACS 2021.5 [50] software package, along with the CHARMM force fields. To generate the initial structural coordinates and topologies for the simulations, the CHARMM-GUI tool was utilized [51-52]. The initial structures underwent energy minimization and equilibration in two stages. The first stage involved an NVT ensemble, maintaining a temperature of 300K, while the second stage involved an NPT ensemble, maintaining a pressure of 1 atm. Each stage lasted for approximately 100 ps. Temperature and pressure were controlled using a Berendsen thermostat and a barostat with relaxation times of $\tau = 0.1$ ps and $\tau = 2.0$ ps, respectively. Once the system achieved equilibration in temperature and pressure, the final production runs were carried out using an NVT ensemble for 50 ns, with a time step of 2 fs for integration of the equations of motion. For the calculation of radial distribution profiles, a bin width of 0.05 nm was employed, extending radially outward from the center of mass of the Al^{3+} ion towards the selected molecule group. These profiles provide insights into the spatial distribution of particles around the selected molecule group.

COMSOL simulation: The distributions of local current density were simulated by

COMSOL Multiphysics software with "tertiary current distribution (Nernst-Planck) interface". The electrochemical reaction kinetics at the electrode-electrolyte interface could be described by using Butler−Volmer equation.

$$i_{loc} = i_0 \left(exp\left(\frac{\alpha_a F \eta}{RT}\right) - exp\left(\frac{\alpha_c F \eta}{RT}\right) \right)$$

Where i_{loc} is the actual exchange current density, i_0 represents exchange current density, α_a is the anodic charge transfer coefficient and α_c is the cathodic one, η is the overpotential, T is the system temperature, and F is the ideal gas constant. The electrolyte/electrode interface was modeled using a 5×4 μm^2 simulation cell (Fig. 4E and F) wherein the top part represents the electrolyte and the bottom part the electrode. In the modeling deposition process, an average current density of 0.1, 1 and 5 mA cm^{-2} were applied to two different simulation systems representing oxidised and Bi-protected Al anode surface. These two systems each had a rugged surface as observed from the SEM (Fig. 2A and B) and differed from each other in terms of surface ionic conductivity, with the conductivity of oxidised Al surface to be one fourth of protected Al.

Supporting Information

Supporting Information is available from the publisher or from the author.

References

[1] Q. Pang, J. Meng, S. Gupta, X. Hong, C. Y. Kwok, J. Zhao, Y. Jin, L. Xu, O. Karahan, Z. Wang, S. Toll, L. Mai, L. F. Nazar, M. Balasubramanian, B. Narayanan, D. R. Sadoway, *Nature* **2022**, 608, 704.

[2] H. Jiang, L. Tang, Y. Fu, S. Wang, S. K. Sandstrom, A. M. Scida, G. Li, D. Hoang, J. J. Hong, N.-C. Chiu, K. C. Stylianou, W. F. Stickle, D. Wang, J. Li, P. A. Greaney, C. Fang, X. Ji, *Nature Sustainability* **2023**, DOI: 10.1038/s41893-023-01092-x.

[3] H. Ding, J. Wang, J. Zhou, C. Wang, B. Lu, *Nat. Commun.* **2023**, 14, 2305.

[4] C. Wang, A. C. Thenuwara, J. Luo, P. P. Shetty, M. T. McDowell, H. Zhu, S. Posada-Pérez, H. Xiong, G. Hautier, W. Li, *Nat. Commun.* **2022**, 13, 4934.

[5] Z. Zhao-Karger, Y. Xiu, Z. Li, A. Reupert, T. Smok, M. Fichtner, *Nat. Commun.* **2022**, 13, 3849.

[6] C. Niu, H. Lee, S. Chen, Q. Li, J. Du, W. Xu, J.-G. Zhang, M. S. Whittingham, J. Xiao, J. Liu, *Nat. Energy* **2019**, 4, 551.

[7] J. Asenbauer, T. Eisenmann, M. Kuenzel, A. Kazzazi, Z. Chen, D. Bresser, *Sustainable Energy & Fuels* **2020**, 4, 5387.

[8] S. K. Das, S. Mahapatra, H. Lahan, *J. Mater. Chem. A* **2017**, 5, 6347.

[9] S. Kumar, R. Satish, V. Verma, H. Ren, P. Kidkhunthod, W. Manalastas, M. Srinivasan, *J. Power Sources* **2019**, 426, 151.

[10] Z. Hu, H. Zhang, H. Wang, F. Zhang, Q. Li, H. Li, *ACS Materials Letters* **2020**, 2, 887.

[11] S. Kumar, P. Rama, G. Yang, W. Y. Lieu, D. Chinnadurai, Z. W. Seh, *Nano-Micro Letters* **2022**, 15, 21.

[12] J. Zheng, D. C. Bock, T. Tang, Q. Zhao, J. Yin, K. R. Tallman, G. Wheeler, X. Liu, Y. Deng, S. Jin, A. C. Marschilok, E. S. Takeuchi, K. J. Takeuchi, L. A. Archer, *Nat. Energy* **2021**, 6, 398.

[13] Q. Zhao, M. J. Zachman, W. I. Al Sadat, J. Zheng, L. F. Kourkoutis, L. Archer, *Sci. Adv.* **2018**, 4, 1.
[14] S. Kumar, T. Salim, V. Verma, W. Manalastas, M. Srinivasan, *Chem. Eng. J.* **2022**, 435, 134742.
[15] S. Kumar, V. Verma, H. Arora, W. Manalastas, M. Srinivasan, *ACS Applied Energy Materials* **2020**, 3, 8627.
[16] K. L. Ng, B. Amrithraj, G. Azimi, *Joule* **2022**, 6, 134.
[17] L. D. Reed, A. Arteaga, E. J. Menke, *J. Phys. Chem. B* **2015**, 119, 12677.
[18] T. Mandai, P. Johansson, *J. Mater. Chem. A* **2015**, 3, 12230.
[19] Z. Slim, E. J. Menke, *J. Phys. Chem. C* **2022**, 126, 2365.
[20] T. Mandai, P. Johansson, *J. Phys. Chem. C* **2016**, 120, 21285.
[21] M. Chiku, S. Matsumura, H. Takeda, E. Higuchi, H. Inoue, *J. Electrochem. Soc.* **2017**, 164, A1841.
[22] X. Wen, J. Zhang, H. Luo, J. Shi, C. Tsay, H. Jiang, Y.-H. Lin, M. A. Schroeder, K. Xu, J. Guo, *J. Phys. Chem.* **2021**, 12, 5903.
[23] X. Zhao, Z. Zhao-Karger, M. Fichtner, X. Shen, *Angew. Chem. Int. Ed.* **2020**, 59, 5902.
[24] Z. Xue, Z. Gao, X. Zhao, *ENERGY & ENVIRONMENTAL MATERIALS* **2022**, 5, 1155.
[25] Q. Zhao, J. Zheng, Y. Deng, L. Archer, *J. Mater. Chem. A* **2020**, 8, 23231.
[26] C. Yan, C. Lv, B.-E. Jia, L. Zhong, X. Cao, X. Guo, H. Liu, W. Xu, D. Liu, L. Yang, J. Liu, H. H. Hng, W. Chen, L. Song, S. Li, Z. Liu, Q. Yan, G. Yu, *J. Am. Chem. Soc.* **2022**, 144, 11444.
[27] Q. Ran, H. Shi, H. Meng, S.-P. Zeng, W.-B. Wan, W. Zhang, Z. Wen, X.-Y. Lang, Q. Jiang, *Nat. Commun.* **2022**, 13, 576.
[28] L. Fu, X. Wang, Z. Chen, Y. Li, E. Mao, Z. W. Seh, Y. Sun, *Carbon Energy* **2022**, 4, 12.
[29] A. Zhou, L. Jiang, J. Yue, Y. Tong, Q. Zhang, Z. Lin, B. Liu, C. Wu, l. suo, Y.-S. Hu, H. Li, L. Chen, *ACS Appl. Mater. Interfaces* **2019**, 11, 41356.
[30] R. Horia, D.-T. Nguyen, A. Y. S. Eng, Z. W. Seh, *Nano Lett.* **2021**, 21, 8220.
[31] D.-T. Nguyen, A. Y. S. Eng, R. Horia, Z. Sofer, A. D. Handoko, M.-F. Ng, Z. W. Seh, *Energy Storage Materials* **2022**, 45, 1120.
[32] L. D. Reed, S. N. Ortiz, M. Xiong, E. J. Menke, *Chem. Commun.* **2015**, 51, 14397.
[33] K. Sato, G. Mori, T. Kiyosu, T. Yaji, K. Nakanishi, T. Ohta, K. Okamoto, Y. Orikasa, *Sci. Rep.* **2020**, 10, 7362.
[34] Y. Zhao, A. Du, S. Dong, F. Jiang, Z. Guo, X. Ge, X. Qu, X. Zhou, G. Cui, *ACS Energy Letters* **2021**, 6, 2594.
[35] G. E. McGuire, G. K. Schweitzer, T. A. Carlson, *lnorg. Chem.* **1973**, 12, 2450.
[36] Y.-C. Kim, H.-H. Park, J. S. Chun, W.-J. Lee, *Thin Solid Films* **1994**, 237, 57.
[37] Y. Okamoto, K. Nagata, T. Adachi, T. Imanaka, K. Inamura, T. Takyu, *J. Phys. Chem.* **1991**, 95, 310.
[38] G. Mattogno, G. Righini, G. Montesperelli, E. Traversa, *Appl. Surf. Sci.* **1993**, 70, 363.
[39] G. Mattogno, G. Righini, G. Montesperelli, E. Traversa, *J. Mater. Res.* **1994**, 9, 1426.
[40] R. Hauert, J. Patscheider, M. Tobler, R. Zehringer, *Surf Sci.* **1993**, 292, 121.
[41] K. Hirakawa, Y. Hashimoto, T. Ikoma, *Appl. Phys. Lett.* **1990**, 57, 2555.
[42] *Russ. J. Electrochem.* **2002**, 38, 1364.
[43] Z. Meng, Z. Li, L. Wang, T. Diemant, D. Bosubabu, Y. Tang, R. Berthelot, Z. Zhao-Karger, M. Fichtner, *ACS Appl. Mater. Interfaces* **2021**, 13, 37044.
[44] A. S. Keefe, S. Buteau, I. G. Hill, J. R. Dahn, *J. Electrochem. Soc.* **2019**, 166, A3272.

[45] Y. Xu, H. Jia, P. Gao, D. E. Galvez-Aranda, S. P. Beltran, X. Cao, P. M. L. Le, J. Liu, M. H. Engelhard, S. Li, G. Ren, J. M. Seminario, P. B. Balbuena, J.-G. Zhang, W. Xu, C. Wang, *Nat. Energy* **2023**, DOI: 10.1038/s41560-023-01361-1.
[46] G. Yang, Y. Li, C. Zhang, J. Wang, Y. Bai, C. Y. J. Lim, M.-F. Ng, Z. Chang, S. Kumar, Z. Sofer, W. Liu, Z. W. Seh, *Nano Lett.* **2022**, 22, 9138.
[47] M. Angell, G. Zhu, M.-C. Lin, Y. Rong, H. Dai, *Adv. Funct. Mater.* **2020**, 30, 1901928.
[48] M. Angell, C.-J. Pan, Y. Rong, C. Yuan, M.-C. Lin, B.-J. Hwang, H. Dai, *Proceedings of the National Academy of Sciences* **2017**, 114, 834.
[49] M.-C. Lin, M. Gong, B. Lu, Y. Wu, D.-Y. Wang, M. Guan, M. Angell, C. Chen, J. Yang, B.-J. Hwang, H. Dai, *Nature* **2015**, 520, 324.
[50] Lindahl, Abraham, Hess, v. d. Spoel, *Zenodo* **2022**, DOI: 10.5281/zenodo.5850051.
[51] S. Kim, J. Lee, S. Jo, C. L. Brooks Iii, H. S. Lee, W. Im, *J. Comput. Chem.* **2017**, 38, 1879.
[52] S. Jo, T. Kim, V. G. Iyer, W. Im, *J. Comput. Chem.* **2008**, 29, 1859.